THE EFFECTS OF WAVE-BREAKING-INDUCED TURBULENCE ON BOTTOM STRESS AND SUSPENDED SEDIMENT TRANSPORT – A 3D NUMERICAL STUDY

Zheyu Zhou, Tian-Jian Hsu,[1] Francis C. K. Ting[2], Xiaofeng Liu[3]

To better understand the effect of wave-breaking-induced turbulence on nearshore sand transport, we carry out a 3D Large Eddy Simulation study of breaking solitary wave in spilling condition. Using a turbulence-resolving approach, we investigate the formation and evolution of wave-breaking-induced turbulent coherent structures, commonly known as obliquely descending eddies (ODEs), and how they may interact with the bed and enhance the suspended sediment transport. The numerical implementation is based on an open-source CFD library of solvers, called OpenFOAM®, where the incompressible 3D filtered Navier-Stokes equations for the water and the air phases are solved with a finite volume scheme. The evolution of the water-air interfaces are approximated with a Volume of Fluid (VOF) method. With the dynamic Smagorinsky closure, the numerical model results show good agreement with measured wave flume data of solitary wave breaking over a 1/50 sloping beach. Simulation results show that 3D hairpin vortices are generated under breaking wave, and they possess counter-rotating and downburst features, which are the key characteristics of obliquely descending eddies (ODEs) observed by earlier laboratory studies with Particle Image Velocimetry. A suspended sediment transport formulation (Liu and Garcia 2008) has been incorporated into the present hydrodynamic solver as part of the OpenFOAM® framework. Model results suggest that those ODEs that impinge onto the bed can cause significant bottom sediment suspension, and the location of the sediment plume is highly associated with the impinging points of ODEs but with notable time-lag.

Keywords: Breaking wave; sediment suspension; Large Eddy Simulation

1.Introduction

Many previous field and laboratory studies of surf zone sediment transport demonstrated that breaking wave-induced turbulence can approach the seabed and results in large amount of sediment suspension (e.g., Ogston & Sternberg 1995; Beach & Sternberg 1995; Voulgaris & Collins 2000; Scott et al. 2009; Aagaard & Hughes 2010; Yoon & Cox 2012). For example, field data of Beach & Sternberg (1995) indicated that the breaker type and the distance from the breakpoint are two main factors governing the suspended sediment concentration in the surf zone. It is generally recognized that the importance of breaking waves has to be incorporated into models of surf zone sediment transport (e.g., Kobayashi and Johnson 2000).

The mechanism of the injection of surface generated turbulence onto the seabed is studied via small-scale laboratory experiments. Pioneering work of Nadaoka et al. (1989) demonstrated the generation and evolution of surface roller into three-dimensional obliquely descending eddies (ODEs), which are capable of penetrating into the water column and approaching the seabed. Several later studies further improved the understanding of this process using Particle Image Velocimetry (PIV) (e.g., Kimmoun & Branger 2007; Ting 2006, 2008; Ting and Nelson 2011). Ting (2008) measured the instantaneous turbulent velocity field under a broken solitary wave with a stereoscopic PIV system. This study revealed that large-scale turbulence first arrived as a downburst of turbulent fluid, and each downburst was accompanied by two counter-rotating vortices. These counter-rotating vortices extend to the free surface in the form of vortex loops which were produced by bending and stretching of primary vortex generated in the wave breaking process, possibly as a result of three-dimensional water surface deformation.

Several 3D numerical simulations were carried out in order to capture the generation and evolution of ODEs (e.g., Christensen and Deigaard 2001; Christensen 2006; Watanabe et al. 2005; Lubin et al. 2006). More recently, Smooth Particle Hydrodynamic (SPH) method has also been adopted to better resolve the high curvature of free surface during the wave breaking process. Farahani and Dalrymple (2013) utilized SPH to resolve the generation and evolution of 3D turbulent coherent structures under

[1] Department of Civil and Environmental Engineering, University of Delaware, 301 DuPont Hall, Newark, Delaware, 19716, USA
[2] Department of Civil and Environmental Engineering, South Dakota State University, Crothers Engineering Hall, Brookings, South Dakota, 57007, USA
[3] Department of Civil and Environmental Engineering, The Pennsylvania State University, 212 Sackett Building, University Park, Pennsylvania, 16802-1408, USA

breaking waves. However, these studies have not focused on the fate of these turbulent coherent structures near the bed.

In order to investigate the turbulent coherent structure induced by breaking wave and their effect on sediment suspension, we carried out a 3D Large Eddy Simulation of wave breaking process over a sloping beach. We first validated the numerical model with laboratory flume study of solitary wave breaking over a 1/50 sloping beach reported by Ting (2006, 2008). Preliminary results of the solitary wave simulations and validation with Synolakis (1987) and Ting (2006, 2008) have been reported in Sangermano (2013). More detailed validation with Ting (2006, 2008) can be found in Zhou et al. (2014). Here, additional simulations are carried out to investigate the interaction between the ODEs and the sediment suspension under a breaking solitary wave in spilling condition.

2.Model Formulation

In this study, a 3D turbulence-resolving approach is adopted via large-eddy simulation (LES). By filtering the Navier-Stokes equations, the flow field is separated into the resolved and the unresolved fields. With appropriate numerical resolution, the generation and the evolution of turbulent coherent structures are resolved (at the resolved scale). The effect of small-scale turbulence is parameterized using a sub-grid scale closure scheme.

2.1 Governing Equations

In LES, the Navier-Stokes equations are filtered in the way that only motions with length-scales greater than the filter scale are solved directly. Here, the flow field is filtered numerically, and the filter length Δ is defined as the characteristic length scale of the grid size:

$$\Delta = \left(\Delta x \cdot \Delta y \cdot \Delta z\right)^{1/3} \tag{1}$$

where Δx , Δy , Δz are the grid size in streamwise, spanwise and vertical directions, respectively. The filtered Navier-Stokes equations are given as:

$$\frac{\partial \overline{u}_i}{\partial x_i} = 0 \tag{2}$$

$$\frac{\partial \overline{u}_i}{\partial t} + \overline{u}_j \frac{\partial \overline{u}_i}{\partial x_j} = -\frac{1}{\rho}\frac{\partial \overline{p}}{\partial x_i} + \upsilon \frac{\partial^2 \overline{u}_i}{\partial x_j \partial x_j} - \frac{\partial}{\partial x_j}\left(\overline{u_i u_j} - \overline{u}_i \overline{u}_j\right) + g_i \tag{3}$$

where i,j =1, 2, 3, $\overline{u}_i$ is the filtered flow velocity, ρ is the fluid density, p is pressure, and ν is the kinematic viscosity of the fluid. Here, an overbar represents a filtered quantity, and the third term on the right-hand-side of equation (3) is the gradient of subgrid stress tensor τ_{ij} , which can be expressed as

$$\tau_{ij} = \overline{u_i}\,\overline{u_j} - \overline{u_i u_j} \tag{4}$$

To solve these equations, we need a closure model for τ_{ij} (see Section 2.2). For the simulation of wave breaking process specifically, both the fields of water and air are solved in the present study using the Volume of Fluid (VOF) method (Hirt and Nichols 1981) and as a result the general representation of fluid density ρ is calculated by

$$\rho = \alpha_1 \rho_1 + \left(1 - \alpha_1\right)\rho_2 \tag{5}$$

in which $\rho_1 = 1000 kg/m^3$ is the density of water, $\rho_2 = 1 kg/m^3$ is the density of air, α_1 is the volume fraction of water contained in a grid cell. The governing equation of the volume fraction α_1 in an immiscible two-fluid system is written as (Hirt and Nichols 1981):

$$\frac{\partial \alpha_1}{\partial t} + \frac{\partial}{\partial x_j}\left(\alpha_1 \overline{u}_{1i}\right) = 0 \tag{6}$$

where $\overline{u}_{1i}$ represents the velocity of the water phase. Grid cells representing the water-air interface are of α_1 ranging between zero and one. When a grid cell is completely occupied by water (or air),

$\alpha_1 = 1$ (or 0). As a result, the exact value of $\overline{u}_{1i}$ for a give interface grid cell cannot be obtained and requires further approximation (e.g., interpolation). This issue is discussed in Rusche (2002) and Klostermann et al. (2012) where more detailed numerical implementation of the present solver is given.

2.2 Sub-grid Closure Model

Calculation of sub-grid scale energy is accomplished by incorporating a closure scheme in the LES that parameterizes the sub-grid turbulent motions. The dynamic Smagorinsky closure model based on the work of Germano (1991) and modified by Lilly (1992) is utilized in the present study. According to the standard Smagorinsky closure, the sub-grid scale viscosity is assumed to be calculated by (e.g., Pope 2000):

$$\nu_{ts} = \left(C_s \Delta\right)^2 \left|\overline{S_{ij}}\right| \tag{7}$$

where $\left|\overline{S_{ij}}\right| = \left(2\overline{S_{ij}}\,\overline{S_{ij}}\right)^{1/2}$ is the magnitude of the strain rate tensor $\overline{S_{ij}}$ obtained from the resolved velocity field and C_s is the Smagorinsky coefficient. The sub-grid stress tensor is solved using the following closure assumption:

$$\tau_{ij} - \frac{1}{3}\delta_{ij}\tau_{kk} = -\nu_{ts} 2\overline{S_{ij}} = 2C_s^2 \Delta^2 \left|\overline{S_{ij}}\right| \overline{S_{ij}} \tag{8}$$

In the standard Smagorinsky closure, C_s is specified as a constant of 0.167. Instead of maintaining a constant C_s, the dynamic Smagorinsky model applies a second test filter $\hat{\Delta}$, which is chosen to be $2\hat{\Delta}$ in the numerical model, to the equations of motion (Lilly, [1992]), yielding a test scale stress tensor of the form

$$T_{ij} - \frac{1}{3}\delta_{ij} T_{kk} = 2C_s^2 \hat{\Delta}^2 \left|\hat{\overline{S}}_{ij}\right| \overline{S_{ij}} \tag{9}$$

where T_{ij} represents the test scale stress. Subtraction of the subgrid scale stress tensor from the test grid scale stress tensor reveals the range of resolved motion between the two scales. A proper value of the dynamic Smagorinsky coefficient C_s is then determined to minimize the discrepancy. In this study, simulation results are primarily presented by using the dynamic Smagorinsky closure.

2.3 Suspended sediment transport

Suspended sediment transport module (Liu and Garcia 2008) has been incorporated into the numerical model recently. The governing equation of sediment volume concentration ϕ is written as

$$\frac{\partial \phi}{\partial t} + \frac{\partial}{\partial x_j}\left[\left(u_i - w_s\right)\phi\right] = \frac{\partial}{\partial x_j}\left[\left(\nu + \nu_{sgs}\right)\frac{\partial \phi}{\partial x_j}\right] \tag{10}$$

where u_i is the fluid velocity, w_s is the sediment settling velocity magnitude, ν is the kinematic viscosity, and ν_{sgs} is the sub-grid scale viscosity. For bottom boundary condition of sediment volume concentration ϕ, we adopt the following Neumann boundary condition

$$\frac{\partial \phi}{\partial z} = -\frac{w_s}{\nu + \nu_{sgs}}\phi_b^* \tag{11}$$

with the reference concentration suggested by Zysermann and Fredsøe (1994):

$$\phi_b^* = \begin{cases} \dfrac{0.331\left(\theta-\theta_{cr}\right)^{1.75}}{1+0.331\dfrac{\left(\theta-\theta_{cr}\right)^{1.75}}{0.46}}, \theta > \theta_{cr} \\ 0, \theta < \theta_{cr} \end{cases} \tag{12}$$

2.4 Boundary conditions

Near-wall modeling has been used in the present study since the numerical resolution in typical wave flume simulation is not sufficient to resolve the viscous sub-layer and buffer layer. Here we ensure the velocity follows the following semi-empirical profile (Spalding, 1961):

$$z^+ = u^+ + \frac{1}{E}\left[e^{\kappa u^+} - 1 - \kappa u^+ - \frac{1}{2}\left(\kappa u^+\right)^2 - \frac{1}{6}\left(\kappa u^+\right)^3\right] \tag{13}$$

where $E = 9.8$, $\kappa = 0.41$, $z^+ = z u_\tau / \nu$, $u^+ = U / u_\tau$ with U as the velocity magnitude and u_τ as the friction velocity. Equation (13) becomes the logarithmic law of the wall for large z^+ and linear profile in the viscous sub-layer for small z^+. Solving Equation (13) iteratively, we can obtain the friction velocity u_τ, which can be used as bottom boundary condition for the momentum equations parallel to the bottom. Moreover, bottom boundary condition for sub-grid scale viscosity is then calculated as

$$\nu_{ts} = \frac{u_\tau^2}{\partial \overline{u} / \partial z} - \nu \tag{14}$$

Solitary wave is sent into the modeled wave flume by specifying time series of free-surface elevation, streamwise and vertical velocity profiles based on the first-order solution of Lee et al. (1982). This is implemented numerically via the groovyBC toolbox (Gschaider, 2009). Periodic boundary conditions are also used here for the two lateral boundaries in the numerical wave flume instead of side walls, similar to many other turbulence-resolving studies (e.g., Vittori and Verzicco 1998; Lubin et al. 2006; Ozdemir et al. 2013). The width of the numerical flume is chosen to ensure that it is much larger than the characteristic size of the largest turbulent coherent structure in the experiment. In this way, the necessary domain width can be smaller than the actual flume width so that higher spatial resolution in the y-direction can be used to better resolve flow turbulence. In addition, by using periodic boundary condition for two lateral boundaries, turbulence statistics can be obtained approximately by spatial averaging over the spanwise (y-) direction.

2.5 Numerical Implementation

The filtered Navier-Stokes equations (2) and (3) are solved by the segregated pressure correction method, following the procedure of Rusche (2002), and Medina (2008) (see also Klostermann et al. 2012). Here, a second-order implicit Crank-Nicolson scheme is used in time integration. For the convection terms, combination of upwind scheme and central difference scheme is adopted (Jasak et al. 1999; Berbervoić et al. 2009; Klostermann et al. 2012). Central difference scheme is used for the gradient and divergence terms. The diffusion term is discretized by approximating face values with central difference scheme, and evaluating the resulting flux through the face with nonorthogonal correction (Jasak 1996). For the simulation of wave breaking process, a boundary-fit domain is used to establish the numerical wave flume in order to better resolve the interaction of turbulent coherent structures with the bed. Volume of Fluid (VOF) method is used to track the air-water interface (Hirt and Nichols 1981). The numerical implementation of the present 3D model is achieved by OpenFOAM, an open-source C++ toolbox for Computational Fluid Dynamics (CFD), which contains a Navier-Stokes equations solver (interFoam) based on a finite volume scheme for two immiscible fluids with an interface tracking capability (Rusche 2002, Klostermann et al. 2012). The numerical model is fully parallelized with Message Passing Interface (MPI).

3.Simulation of solitary wave breaking over 1/50 sloping beach

3.1 Model validation

In Ting (2006, 2008), the laboratory flume is of 25 m long by 0.90 m wide by 0.75 m deep with a constant slope of 1/50 extending the length of the flume. With a still water depth of $h_0 = 0.3m$, a highly nonlinear solitary wave of initial wave height $H = 0.22m$ is sent into the flume via the left boundary. In the physical experiment, free surface evolution was recorded by twelve resistant-type wave gauges placed in different streamwise locations in the wave flume. Five ADVs located at different elevations record time series of three component velocities at 25 Hz at a fixed streamwise location near the breaking point (x=7.37 m from the wave maker).

In the numerical simulation, the wave flume was replicated with minor modifications (see figure 1). The same 1/50 constant slope is maintained. However, in order to save computational time and memory use, the dry beach region at the right end of the flume has been shortened. The numerical wave flume dimensions are hence specified as 18.2 m long by 0.60 m wide by 0.60 m deep. In this study, our primarily focus is on the first 9 sec of the experiment. The simulation results analyzed here are not affected by the shortened wave flume. The width of the numerical wave flume is 0.6 m, which is 0.3 m narrower than that of the physical wave flume. The size of the largest measured and predicted turbulent coherent structure is around 10~15 cm, which is much smaller than the modeled flume width.

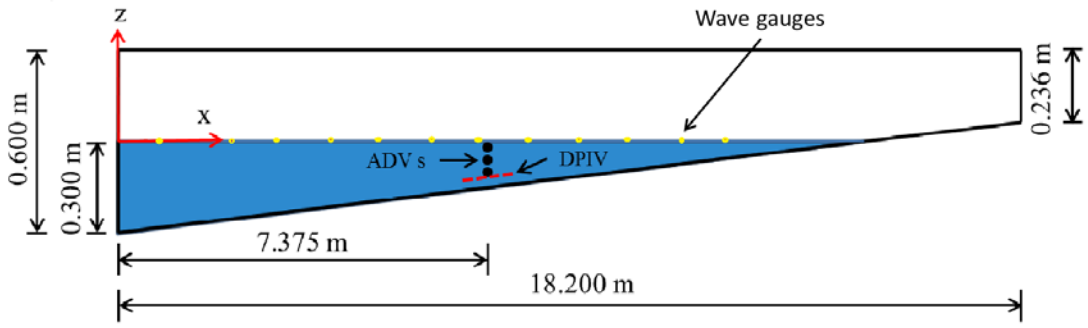

Figure 1. A schematic plot of the side view of the numerical wave flume with sensor locations similar to the laboratory flume experiment of Ting (2006, 2008).

In Ting (2006, 2008), the same physical experiment is carried out 29 times for ADV measurements and at least 5 times for wave height measurements. Hence, we adopted Reynolds decomposition to separate the flow field into turbulence-averaged component and fluctuating component. For example, the flow velocity is decomposed into:

$$u_i = \langle u_i \rangle + u_i' \tag{15}$$

with $\langle\ \rangle$ the turbulence-average operator, $\langle u_i \rangle$ the turbulence-averaged velocity, and u_i' the velocity fluctuations. By implementing periodic boundary condition for two lateral boundaries in the numerical simulation, the computed flow field is averaged over the spanwise direction to obtain approximated flow statistics (e.g., Vittori and Verzicco 1998; Ozdemir et al. 2013). Due to finite domain width, some uncertainties may arise when directly comparing Reynolds-averaged flow statistics between the measured data and model results.

The model domain consists of 2427, 80 and 80 grid points in the streamwise (x), spanwise (y), and vertical (z) directions, respectively, and a total number of N=15,532,800 computational cells are used. The smallest (largest) grid size are 4.6 mm (11.5 mm) in the streamwise direction and 3 mm (7.5 mm)

in the vertical direction, respectively. Uniform grid with the size of 7.5 mm is specified in the spanwise direction. The origin of the streamwise (x), spanwise (y) and vertical (z) axes are defined at the wave maker, the right boundary of the flume (when facing onshore) and the initial still water level, respectively (see Figure 1). Along the wave flume, free-surface elevation are recorded at 12 locations (x = 0.55, 2.2, 3.2, 4.25, 5.25, 6.25, 7.25, 8.25, 9.25, 10.3, 11.3, and 12.3 m). The comparisons of temporal evolutions of free-surface elevation between model results and measured data are presented in Figure 2. In general, the numerical model captures well the temporal evolution of wave shape before and after the wave breaks. In terms of maximum wave height, the predicted wave breaks slightly earlier than the measured data. Also, the predicted wave height is slightly larger than the measured data as the broken wave start to evolve into a bore (see Figure 2(g) to (h)).

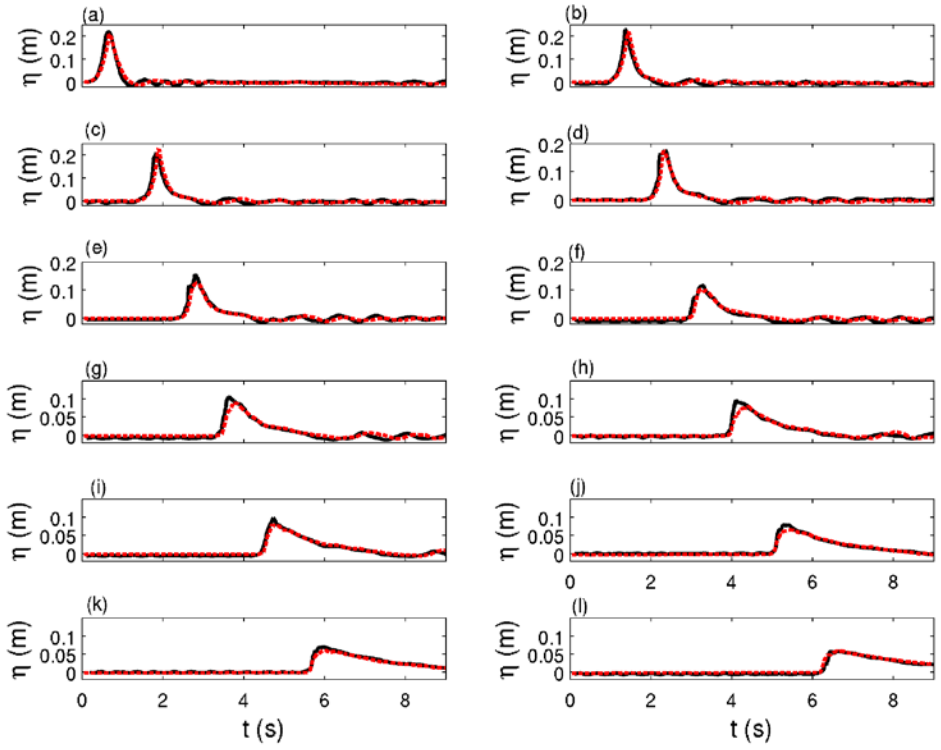

Figure 2. Comparisons of time series of free-surface elevation between the model results (solid curves) and measured data (dashed curves). Time series at (a) x = 0.55m; (b) x = 2.2m; (c) x = 3.2m; (d) x = 4.25m; (e) x = 5.25m; (f) x = 6.25m; (g) x = 7.25m; (h) x = 8.25m; (i) x = 9.25m; (j) x = 10.3m; (k) x = 11.3m; (l) x = 12.3m.

Measurements of flow velocity at x=7.375 m (local water depth is h=15.25 cm) are taken for five vertical locations. This is the location where intense turbulent coherent structures penetrate into the water column after initial overturning of the breaking solitary wave. The predicted averaged streamwise flow velocity agrees very well with the measured data. In terms of the RMS velocity fluctuation in three directions, model is also able to capture the temporal evolution and the magnitude under the broken wave. Finally, the model is able to predict the evolution of ODEs approaching the bed. By examining the snapshots of fluctuating velocity field and vorticity field (see also Figure 4), it is clear that the counter-rotating and downburst features are captured by the numerical simulation similar to observed data presented by Ting (2008). More detailed comparison of the averaged velocity and RMS velocity fluctuations are discussed in Zhou et al. (2014) and they are not repeated here. The remaining of this paper will focus on preliminary investigation on the interaction of ODEs with suspended sediments.

3.2 Formation and Characterization of Obliquely Descending Eddies

In this study, we adopt the λ_2 method (Jeong and Hussein 1995) to investigate the formation and characterization of turbulent coherent structures under the breaking solitary wave. Figure 3 (a) presents the instantaneous image of iso-surfaces of air-water interface (represented by blue surfaces with α_1=0.5)

and iso-surfaces of λ_2=-50 (represented by yellow surfaces) at t = 5.0 sec. It is evident that the flow field is populated with many 3D turbulent coherent structures with local irregularities in terms of intensity and shape. At the same time, a couple of intense coherent structures are penetrating through the water column, and some of them have already interacted with the bed and induced sediment suspension (more detailed discussion on sediment suspension will be presented in the next Section). Moreover, these intense turbulent coherent structures are what commonly recognized as hairpin vortices in turbulent shear flows (but the orientation is reversed in the present problem). Similar vortex structures under breaking wave have also been reported by Watanabe et al. (2005) with LES approach and Farahani and Dalrymple (2013) with SPH approach. In the study of Farahani and Dalrymple (2013), this vortex structure is named as reversed horseshoe vortex. More description and discussion about the generation, evolution, and the fate of turbulent coherent structures can be found in Zhou et al. (2014).

Although the qualitative visualization of vortices using λ_2 method shows that some of the 3D turbulent coherent structures are indeed able to approach the bed, quantitative analyses are still needed to diagnose whether they are the obliquely descending eddies (ODEs) observed in the laboratory experiments (e.g., Nadaoka et al. 1989; Ting 2008; Huang et al. 2012). Here, we study the detailed structure of single turbulent coherent structure and compare it with the structure of the ODEs observed in laboratory experiment. With the particle imaging velocimetry (PIV), Ting (2006, 2008) are able to measure the detailed flow field of ODEs near the bed. In the experiment, the observed ODEs consist of a pair of counter-rotating, vertically-oriented vortex pair. Between the cores of these two vortices are an uprush and a downrush of fluid represented by volumes of strong positive and negative turbulent vertical velocity fluctuation. As a result of the proximity of the uprush and downrush of fluid, a high shear region is generated, and it in turn shows high level of turbulent kinetic energy.

In the current study we present the numerical results for instantaneous vertical vorticity ω_z, velocity fluctuation in the vertical direction w', and turbulent kinetic energy (per unit mass) k (see Figure 4) of a hairpin vortex located at the plane 60 mm above the bed at t = 4.3 sec. From ω_z shown in Figure 4a, it is evident that the hairpin vortex observed in the simulation also has the counter-rotating feature with negative (positive) vertical vorticity on the right (left) side of the panel. Between the cores of these vertical voticities, there is a strong downrush of flow with velocity fluctuation exceeding 0.4 m/s (see Figure 4b), and at the same location, region of high instantaneous TKE can also be observed (see Figure 4c). Qualitatively, the main characteristics of the ODEs predicted by the numerical simulation are very similar to the PIV observations in Ting (2008). Furthermore, the numerical results also indicate that the so-called obliquely descending eddies are essentially the downrush of hairpin vortices under breaking waves. Similar features of such ODE (or reversed hairpin vortex) are also observed at other elevations (Zhou et al. 2014).

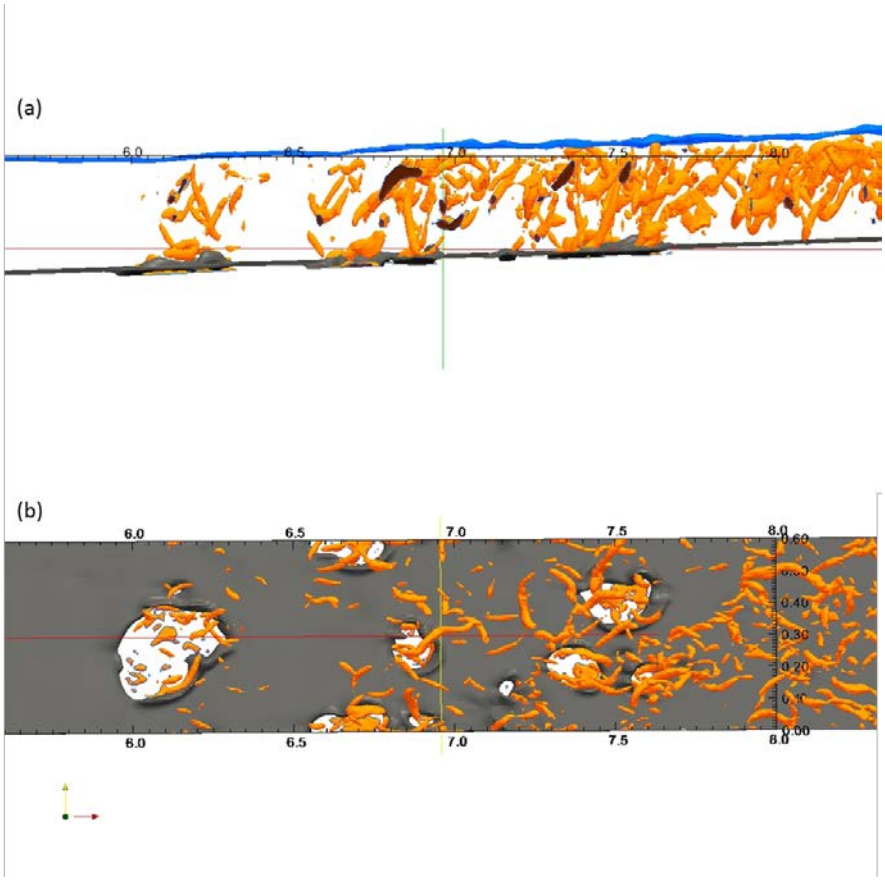

Figure 3. Turbulent coherent structures and suspended sediment under the breaking solitary wave at t = 5.0 sec visualized by λ_2 method, (a) side view; (b) top view with the free surface removed. The blue iso-surfaces are the free surface represented by α_1=0.5. The yellow iso-surfaces represent λ_2=-50. The dark gray iso-surfaces represent sediment concentration of 0.5 %.

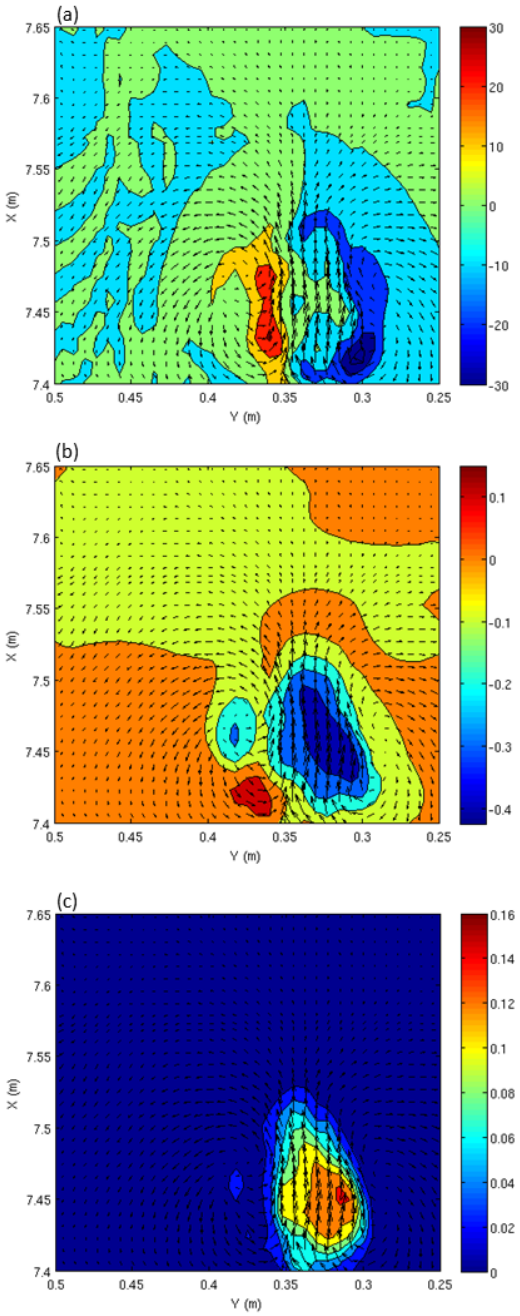

Figure 4. An x-y plane snapshot (view from the top) of an obliquely descending eddy at t = 4.3 sec and 60 mm above the bed. (a) instantaneous vorticity in the z-direction (s^{-1}); (b) vertical velocity fluctuation (m/s); (c) instantaneous turbulent kinetic energy per unit mass (m^2/s^2).

3.3 Interaction between Obliquely Descending Eddies and Suspended Sediment

Validation of the sediment suspension module with the sheet flow data of Sumer et al. (1996) for steady channel flow and O'Donoghue et al. (2004) for oscillatory flow is being carried out. Given the evidence of ODEs interacting with the bed, further investigation into the details of this process is warranted. Here, we focus on the effects of ODEs on the bottom sediment suspension.

Based on the numerical simulation of breaking solitary wave in Section 3, fine sediment with median grain size of 63 μm has been used. Sediment is resuspended from the bed via equation (11). In addition to the iso-surface of turbulent coherent structures of $\lambda_2 = -50$ presented in Figure 3b, the iso-surface of sediment volume concentration of 0.5% is also shown (see the iso-surfaces with dark gray color). It is clear that the impingement of ODEs can suspend sediment, since the locations of the sediment plumes coincide with the locations of the impinging ODEs. The sediment plumes exhibit 3D features clearly. Moreover, simulation results show that strong suspension occurs at the edge of the ODE impinging region, while inside the impinging region, suspended sediment concentration is smaller, leaving a void-like zone in each impingement (see Figure 3b). This is due to the downburst discussed in Section 3.2. There is a region of intense downward vertical velocity fluctuation of fluid between the cores of the counter-rotating vortices in an ODE. As a result, inside the impinging region, even if the local sediment can be mobilized, it cannot be suspended up. However, this downburst is accompanied by uprush in the adjacent region, sediment at the edge of the impinging region can be suspended higher into the water column. More detailed investigation of the interaction between ODEs and sediment suspension will be carried out in the near future.

4 Conclusion

A 3D large-eddy simulation study has been carried out in order to investigate the generation and evolution of turbulent coherent structures under a breaking solitary wave and their interaction with the sediment suspension at the bed. The numerical model has been validated with measured data of Ting (2006, 2008) in a laboratory wave flume in terms of free-surface elevation, turbulence-averaged flow velocity and RMS turbulent velocity fluctuations (Zhou et al. 2014). Simulation results show that the turbulent coherent structures under the breaking wave appear to be (reversed) hairpin vortices which can penetrate into the water column. Detailed examination of the instantaneous flow field suggests that these hairpin vortices show counter-rotating and downburst features similar to those observed in Ting (2008). The observed hairpin vortices are also similar to the reversed horseshoe vortices under the breaking wave reported by Farahani and Dalrymple (2013) using the SPH approach. Many of the hairpin vortices are sufficiently intense to impinge onto the bed and enhance sediment suspension. For future work, the numerical model has been further validated with other wave conditions, such as measured free-surface elevation and velocity profiles of a dam-break wave reported by O'Donoghue et al. (2010). The numerical simulation study will also be extended to periodic wave breaking over a slope in large wave flumes in order to investigate the effect of wave-breaking turbulence on enhanced sediment transport rate and direction.

ACKNOWLEDGMENTS

This study is supported by National Sceince Foundation (CMMI-1135026; OCE-1356855) and Office of Naval Research (N00014-14-1-0586). Simulations presented in this paper are carried out on CHIMERA at the University of Delaware with funding supported by the National Science Foundation (CNS-0958512). We gratefully acknowledge researchers involved in developing OpenFOAM®.

REFERENCES

Aagaard, T., and M.G. Hughes. 2010. Breaker turbulence and sediment suspension in the surf zone, *Marine Geology*, 271, 250-259

Beach, R.A., and R.W. Sternberg. 1996. Suspended-sediment transport in the surf zone: response to breaking waves. *Continental Shelf Research*, Vol. 16, No. 15, 1989-2003.

Berbervoić, E., N.P. van Hinsberg, S. Jakirlić, I.V. Roisman, C. Tropea. 2009. Drop impact onto a liquid layer of finite thickness: Dynamics of the cavity evolution, *Physical Review E* 79, 036306

Berbervoić, E. 2010. Investigation of free-surface flow associated with drop impact: numerical simulations and theoretical modeling, *Ph.D. thesis*, Technische Universität Darmstadt.

Chang, K. A., and P. L.-F Liu. 1998. Velocity, acceleration and vorticity under a breaking wave, *Phys. Fluids*, 10(1), 327-329.

Christensen, E.D. and R. Deigaard. 2001. Large eddy simulation of breaking waves, *Coastal Engineering*, 42, 53-86.

Christensen. E.D. 2006. Large eddy simulation of spilling and plunging breakers, *Coastal Engineering*, 53, 463-485.

Deshpande, S.S., L. Anumolu, M.F. Trujillo. 2012. Evaluating the performance of the two-phase flow solver interFoam. *Computational Science & Discovery* 5 (2012) 014016 (36pp).
Farahani, R. J. and R.A. Dalrymple. 2013. Three-dimensional reversed horseshoe vortex structures under broken solitary waves, *Coastal Engineering*, 91, 261-279.
Germano, M., U. Piomelli, P. Moin, W. Cabot. 1991 A dynamic subgrid-scale eddy viscosity model, *Physics of Fluids A*, 3, 1760-1765.
Grasso, F., B. Castelle, B.G. Ruessink. 2012. Turbulence dissipation under breaking waves and bores in a natural surf zone. *Continental Shelf Research,* 43, 133-141.
Gschaider, B. 2009 Contrib groovyBC. *OpenFOAM Wiki.,* http://openfoamwiki.net/index.php/Contrib_groovyBC
Hirt, C.W., and B.D. Nichols. 1981. Volume of fluid (VOF) method for the dynamics of free boundaries. *Journal of Computational Physics*, 39, 201-225.
Huang, Z.C., H.H. Hwung, S.C. Hsiao, K.A. Chang. 2010. Laboratory observation of boundary layer flow under spilling breakers in surf zone using particle image velocimetry. *Coastal Engineering*, 57, 343-357.
Jasak, H. 1996 Error analysis and estimation for the finite volume method with application to fluid flows. *Ph.D. thesis*, Imperial College London.
Jasak, H., H.G. Weller, A.D. Gosman. 1999. High resolution NVD differencing scheme for arbitrarily unstructured meshes. *International Journal for Numerical Methods in Fluids,* 31, 431-449.
Jeong, J., and F. Hussain. 1995. On the identification of a vortex. *Journal of Fluid Mechanics,* 285, 69-94.
Kimmoun, O., and H. Branger. 2007. A particle image velocimetry investigation on laboratory surf-zone breaking waves over a sloping beach. *Journal of Fluid Mechanics,* vol. 588, 353-397.
Klostermann, J., K. Schaake, R. Schwarze. 2012. Numerical simulation of a single rising bubble by VOF with surface compression. *International Journal for Numerical Methods in Fluids,* Vol.71, Issue 8, 960-982.
Lee, J.-J., J.E. Skjelbreia, F. Raichlen. 1982. Measurement of velocities in solitary waves. *Journal of Waterway, Port, Coastal, and Ocean Division,* 108(2), 202-218.
Lilly, D.K. 1992. A proposed modification of the germane subgrid-scale closure method. *Physics of Fluids A,* 4, 633-635.
Liu, X., and M. Garcia. 2008. Three-dimensional numerical model with free water surface and mesh deformation for local sediment scour. *Journal of Waterway, Port, Coastal, and Ocean Engineering,* vol. 134, issue 4.
Lubin, P., S. Vincent, S. Abadie, J.-P. Caltagirone. 2006. Three-dimensional Large Eddy Simulation of air entrainment under plunging breaking waves. *Coastal Engineering*, 53, 631-655.
Nadaoka, K., Hino, M., Koyano Y. 1989 Structure of the turbulent flow field under breaking waves in the surf zone. *Journal of Fluid Mechanics,* 204, 359-387
O'Donoghue, T., and S. Wright. 2004. Concentrations in oscillatory sheet flow for well sorted and graded sand. *Coastal Engineering*, vol. 50, no. 3, pp. 117-138.
O'Donoghue, T., D. Polrajac, L.J. Hondebrink. 2010. Laboratory and numerical study of dambreak-generated swash on impermeable slopes. *Coastal Engineering,* vol.57, no. 5, pp. 513 – 530.
Ogston, A.S., and R.W. Sternberg. 1995 On the importance of nearbed sediment flux measurements for estimating sediment transport in the surf zone. *Continental Shelf Research,* 15, No. 13. 1515-1524.
Ozdemir, C.E., T.-J. Hsu, S. Balachander. 2013. Direct numerical simulations of instability and boundary layer turbulence under a solitary wave. *Journal of Fluid Mechanics*, 731, 545-578.
Pope, S.B. 2000. *Turbulent flows.* Cambridge, UK, Cambridge Univ. Press
Ruessink, B.G., Y. Kuriyama, A.J.H.M. Reniers, J.A. Roelvink, D.J.R. Walstra. 2007. Modeling cross-shore sandbar behavior on the timescale of weeks. *Journal of Geophysical Research,* Vol. 112, F03010.
Rusche, H. 2002. Computational fluid dynamics of dispersed two-phase flows at high phase fractions. *PhD Thesis,* Imperial College of Science, Technology and Medicine, London, England.
Sangermano, J.J. 2013. A numerical study of wave-breaking turbulence beneath solitary waves using large eddy simulation. *Master Thesis,* University of Delaware, Newark, Delaware, USA
Scott N.V., T.-J. Hsu, D. Cox. 2009. Steep wave, turbulence, and sediment concentration statistics beneath a breaking wave field and their implications for sediment transport. *Continental Shelf Research*, 29, 2303-2317

Spalding D.B. 1961 A single formula for the law of the wall. *Journal of Applied Mechanics, Trans. ASME, Series E,* Vol. 28, 455-458
Sumer, B.M.,M.B. Sen, I. Karagali, B. Ceren, J. FredsØe, M. Sottile, L. Zilioli, D.R. Fuhrman. 2011. Flow and sediment transport induced by a plunging solitary wave. *Journal of Geophysical Research,* Vol.116, C01008.
Synolakis, C.E. 1987. The runup of solitary waves. *Journal of Fluid Mechanics,* 185, 523-545.
Ting, F.C.K. 2006. Large-scale turbulence under a solitary wave. *Coastal Engineering*, 53, 441-462.
Ting, F. C.K. 2008. Large-scale turbulence under a solitary wave: Part 2 Forms and evolution of coherent structures. *Coastal Engineering,* 55, 522-536.
Van Leer, B. 1974. Towards the ultimate conservative difference scheme. IV. Monotonicity and conservation combined in a second order scheme. *Journal of Computational Physics,* 14,361-370.
Vittori, G., Verzicco, R. 1998. Direct simulation of transition in an oscillatory boundary layer. *Journal of Fluid Mechanics,* 371,207-232.
Voulgaris, G., and M.B. Collins. 2000. Sediment resuspension on beaches: response to breaking waves. *Marine Geology,* 167, 167-187.
Watanabe, Y., H. Saeki, R.J. Hosking. 2005. Three-dimensional vortex structures under breaking waves. *Journal of Fluid Mechanics,* 545, 291-328.
Weller, H.G. 2008. A new approach to VOF-based interface capturing methods for incompressible and compressible flow. *Technical Report TR/HGW/04,* OpenCFD Ltd.
Yoon, H.-D., and D.T. Cox. 2012. Cross-shore variation of intermittent sediment suspension and turbulence induced by depth-limited wave breaking. *Continental Shelf Research,* 47, 93-106.
Zhou, Z., J. Sangermano, T.-J. Hsu., F.C.K. Ting. 2014. A numerical investigation of wave-breaking-induced turbulent coherent structure under a solitary wave. *Journal of Geophysical Research,* accepted.